



Improvement of the sub-grid-scale model designed for 3D numerical simulation of solid oxide fuel cell electrodes using an adaptive power index

Masashi Kishimoto*, Hiroshi Iwai, Kosuke Miyawaki, Motohiro Saito, Hideo Yoshida

Department of Aeronautics and Astronautics, Kyoto University, Yoshida Honmachi, Sakyo-ku, Kyoto 606-8501, Japan

HIGHLIGHTS

- 3D numerical simulation with real anode microstructure is conducted.
- Sub-grid-scale model is applied to improve the simulation accuracy.
- Adaptive power index is introduced to the SGS model.
- We succeed in reducing computation cost without losing simulation accuracy.

ARTICLE INFO

Article history:

Received 25 July 2012

Received in revised form

17 September 2012

Accepted 19 September 2012

Available online 27 September 2012

Keywords:

Solid oxide fuel cell

Porous electrode

Numerical simulation

Sub-grid-scale model

Microstructure

FIB-SEM

ABSTRACT

Improving the accuracy of the sub-grid-scale (SGS) model designed for three-dimensional (3D) numerical simulation of solid oxide fuel cell (SOFC) electrodes is accomplished by introducing an adaptive power index, which is determined by the length ratio between the grid size and the characteristic scale of the original porous structure. The main function of the SGS model is to maintain the quality of the voxel-based structural information in a resampled structure used as the calculation grid system by considering a structure with a characteristic scale that is smaller than the grid size. Improvement of the simulation accuracy and reduction of the computational load can be expected with the SGS models. In this study, four types of SGS models are investigated to clarify their effect and applicability. They are featured by (1) volume conservation, (2) interfacial connectivity, (3) power law with a constant power index, and (4) power law with an adaptive power index, respectively. The latter two models are based on a power-law expression of the local tortuosity factor and are newly proposed in this study. Although the first three models have a positive contribution to maintain the structural information in the resampled structure, their applicability is not completely assured in a wide range of grid sizes. In the last model, we introduce a length ratio between the grid size and the characteristic scale of the original porous structure in order to let the model exert its effect preferably in accordance with the grid size. The model successfully represents the original structural information in a wide range of grid sizes and improves the simulation accuracy within the given computational resources.

© 2012 Elsevier B.V. All rights reserved.

1. Introduction

Solid oxide fuel cells (SOFCs) are promising energy conversion systems because of their high efficiency and fuel flexibility. Electrodes of the SOFCs mainly consist of porous materials, and their microstructure has a significant influence on the electrode performance. Moreover, performance degradation, which is a significant barrier to the commercialization of SOFCs, is often attributed to the morphologic changes in the porous structure [1–7], such as

sintering and redox of metal catalyst and carbon deposition. Therefore, there is a strong demand to clarify the effect of the microstructure on the performance and durability of the electrodes.

Numerical simulation is one of the most powerful and effective approaches to investigate the microstructural effect on the performance [8–14]. Various phenomena occurring inside the electrodes, such as electron/ion conduction in the solid phases, gas diffusion in the pore phase, and electrochemical reaction at the three-phase boundary (TPB), are analyzed, and the macroscopic performance of the electrodes is predicted.

The accuracy of the numerical simulation basically depends on two aspects: the electrochemical reaction model and the structure model. For the modeling of the electrochemical reaction around the

* Corresponding author. Tel./fax: +81 75 753 5203.

E-mail address: masashi.k.0204@gmail.com (M. Kishimoto).

TPB, many experimental approaches have been conducted focusing on the elementary electrochemical reaction on the catalytic surface in the electrodes [15–19]. Some of the findings were summarized into numerical models, which are available for the numerical simulation [20–23]. For the structure model, on the other hand, many porous models have been developed to mimic the complex electrode microstructure [21,24–26]. For example, the random-spherical packing model [24,25] assumes that the porous structure is composed of two kinds of spheres, representing electron-conductive particles and ion-conductive particles, which are randomly distributed in the field. From the obtained structure, microstructural parameters such as phase connectivity and TPB density can be obtained. However, these structure models require assumptions for the structural configuration, and hence, they cannot always represent the heterogeneous nature of the complex porous structure.

Recently, with state-of-the-art observation techniques such as scanning electron microscopy combined with focused ion beam milling (FIB-SEM) and X-ray computed tomography, the three-dimensional (3D) structure of real porous electrodes can be obtained at nano-scale resolution [1,2,4,6,27–31]. A simulation technique using the obtained 3D structure has also been recently developed [8,9,12–14]. In such 3D analyses, however, the computational load often becomes a critical issue when we use the obtained voxel-based structure for the numerical grid system. The elemental image voxel in the FIB-SEM observation is usually several tens of nanometers in size; therefore, the total number of grids tends to reach to the order of a hundred million, which is unrealistic for the grid system considering the available computational resources. Currently, it is a common practice to resample the original voxel-based data set to reduce the number of calculation grid. The resampling process, however, raises a question as to whether the resampled data set is still a good representation of the original microstructure because it inevitably results in the loss of structural information that is smaller than the calculation grid size (sub-grid-scale information). In our previous report [14], we proposed the use of a sub-grid-scale (SGS) model in order to maintain the quality of the original structural information intact in the resampled structure used for the calculation grid system. In the proposed SGS models, the local transport coefficients in the grids are evaluated with the local information of the porous structure, such as the volume fractions and structural complexity. The effect of the SGS models was investigated through the diffusion and overpotential analyses. We found that if the structural complexity inside each calculation grid is reasonably taken into account, the transport flux of various species in the porous structure can be properly evaluated; hence, a reasonable value of the overpotential can be obtained even when resampling is involved in the grid generation. However, the SGS models examined in our previous report did not always exert the desirable effect in a wide range of grid sizes: the effect was not enough when a coarser grid system was applied or was more than what was required in some other cases.

The aim of this study is to establish more sophisticated SGS models for the 3D numerical simulation in the porous structure and expand its applicability limit. The local structural complexity inside a grid is evaluated by the power of the volume fraction of a porous component (power law), which has been often used in the conventional porous models [24,25]. Moreover, in order to include the effect of the grid size, we introduce an adaptive power index considering the relationship between the grid size and the characteristic scale of the porous structure (power law with an adaptive power index). The effect of the SGS model on the numerical simulation is extensively investigated through the diffusion analysis in the porous structure, and their effect and applicability are evaluated.

2. FIB-SEM observation

2.1. Sample preparation

In this study, a conventional Ni-YSZ cermet is used as a sample porous structure representing the SOFC anode. The fabrication process is as follows: first, NiO powder (Wako Pure Chemical Industries, Ltd.) and YSZ powder (Tosoh Co.) are mixed and ball-milled with zirconia balls (Ø4.0 mm) for 24 h along with ethanol to disperse the particles. After the milling, the ethanol is evaporated using a hot stirrer, and the resultant powder is pre-sintered at 1400 °C for 5 h. It is subsequently ground for 3 h and mixed with polyethylene glycol to form a slurry. Finally, the anode slurry is screen-printed on a disk YSZ electrolyte (Tosoh Co., 24 mm in diameter, 500 µm in thickness) and sintered at 1400 °C for 5 h. The thickness of the anode is around 30 µm. The fabricated NiO-YSZ cermet is reduced under pure hydrogen atmosphere at 1000 °C for 1 h and then cooled down in a reductive atmosphere. We prepare anodes with three different compositions: Ni:YSZ = 30:70, 50:50, and 70:30 vol.%. The reduced anode is infiltrated with epoxy resin (Marumoto Struers KK) under vacuum condition so that the pores of the electrode can be easily distinguished during the SEM observation. The infiltrated sample is cut and mechanically polished with sandpaper and diamond paste to prepare them for the FIB-SEM observation.

2.2. Observation

The 3D microstructure of the Ni-YSZ anodes is observed using the FIB-SEM system. An in-lens secondary electron detector is used for the microstructural observation with an acceleration voltage of ~2 kV. Fig. 1(a) shows an example of the obtained cross-sectional images, in which the white, gray, and black parts correspond to Ni, YSZ, and the pore phase, respectively. In this study, orthogonal coordinate axes X and Y are embedded on the 2D SEM image and Z is the proceeding direction of the FIB milling.

We extract regions available for the numerical analysis and conduct a phase separation based on the image brightness. After the alignment and the phase separation, the sequential set of the 2D images is lined up with the actual increment in the FIB-SEM observation and the 3D porous microstructure is reconstructed in a virtual field. Fig. 1(b) shows the reconstructed microstructure of the porous anode (Ni:YSZ = 50:50). We use the commercial image processing software Avizo (Mercury Computer Systems, Inc.) for the phase separation, 3D reconstruction, and some of the quantification of the porous structure.

3. Numerical model

We conduct a numerical simulation with the 3D porous anodes obtained by the FIB-SEM. In order to evaluate the proposed SGS models in terms of how precisely they can maintain the structural information of the original porous structure, an index is required to characterize both the original porous structure and the resampled structure used for the calculation grid system. For this purpose, the tortuosity factor is the most appropriate microstructural parameter because it directly represents the complexity of the porous structure. We apply different quantification methods for the original porous structure and the resampled structure as follows.

For the original porous structure, we apply the random-walk-based diffusion simulation (RW) [10,32]. This method is specialized for evaluating the tortuosity factor from the voxel-based structure data such as that obtained by the FIB-SEM. Since the requirement for the computational resources is much smaller than

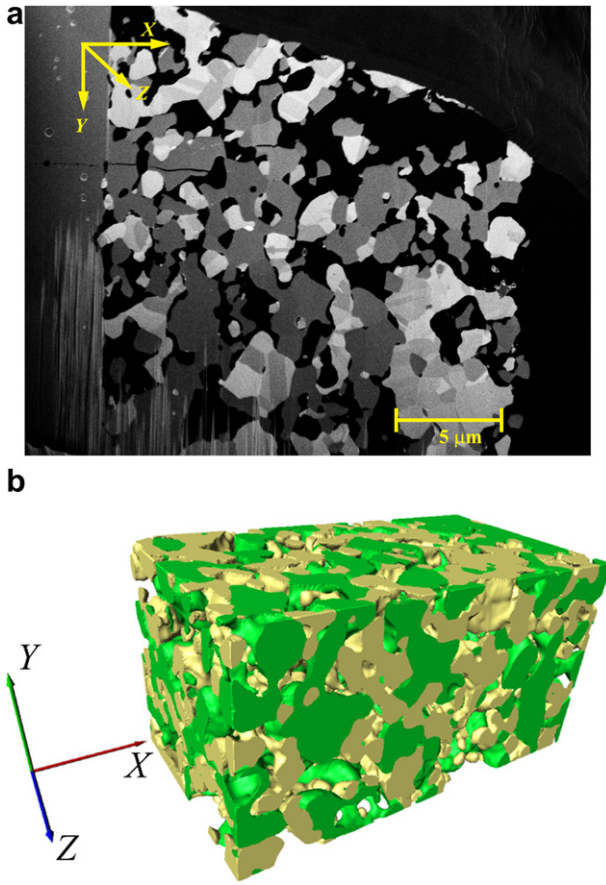


Fig. 1. FIB-SEM observation of the SOFC porous anode. (a) Example of the cross-sectional images (Ni:YSZ = 50:50, white: Ni, gray: YSZ, black: pore). (b) Reconstructed 3D structure (Ni:YSZ = 50:50) (Green:Ni, Yellow:YSZ). (For interpretation of the references to color in this figure legend, the reader is referred to the web version of this article.)

that for the other approaches, resampling is not necessary. The accuracy of this method has been proved in our previous report [29] by comparing the results with those obtained by the lattice Boltzmann method (LBM). Therefore, the tortuosity factor obtained by the random-walk simulation truly represents the structural complexity of the original porous structure. In the later discussion, we use the values obtained from this simulation as a reference.

For the resampled structure used as the grid system, on the other hand, we apply the diffusion simulation based on the finite volume method (FVM) aided by various SGS models. Although our in-house code is capable of conducting the overpotential analysis by considering the electrochemical reaction at the TPB [14], only transport analysis is enough to investigate the effect of the proposed SGS models. Fig. 2 shows the schematic diagram of the grid generation for the FVM analysis using the SGS models. As is often adopted in most studies, the original porous structure is resampled to have a lower spatial resolution. The unique strategy used in our study is that the structural information inside the grid is reflected onto the resampled structure in the form of effective transport coefficients such as effective conductivities and diffusivities.

In the figure, the following length ratio is introduced as a parameter to generally evaluate the grid size:

$$\frac{L_l}{L_{\text{grid}}} \quad (1)$$

where L_l is the characteristic scale of the phase l , such as the particle/pore size, and L_{grid} is the grid size used in the simulation, which is defined as follows:

$$L_{\text{grid}} = \sqrt[3]{\Delta x \Delta y \Delta z} \quad (2)$$

where Δx , Δy , and Δz are the grid sizes in each direction. The value of L_l/L_{grid} is interpreted as the number of grids that are used to resolve a typical structure of a porous material, in other words, one particle. If the grid size is smaller or L_l/L_{grid} is larger, we can expect that the grid-scale information (resampled structure without the SGS model) represents the structural complexity. On the other hand, if the grid size is larger or L_l/L_{grid} is smaller, the proposed SGS models need to exert their effects to maintain the sub-grid-scale information in the resampled structure.

If the tortuosity factor obtained by the FVM-based diffusion simulation is the same as that obtained by the random-walk simulation, we can judge that the resampled structure reasonably maintains the quality of the original structure.

3.1. Random-walk-based diffusion simulation

The tortuosity factor of the original porous structure is quantified by the diffusion simulation based on the random-walk process. In the first step of this method, a large number of imaginary particles are randomly distributed in the considered phase, i.e., the Ni, YSZ, or pore phase. Then, each walker randomly chooses one of the neighboring voxels as its possible location in the next time step. If the selected neighboring voxel is the same as the considered phase, the walker migrates to the voxel. If the selected voxel is a different phase, the walker stays at the current voxel and waits for the next time step. In this procedure, neither absorption nor desorption on the phase boundaries is considered. While repeating this process, the mean square displacement of the random walkers is calculated as follows:

$$\langle r^2(t) \rangle = \frac{1}{N} \sum_{n=1}^N \left[(x_n(t) - x_n(0))^2 + (y_n(t) - y_n(0))^2 + (z_n(t) - z_n(0))^2 \right] \quad (3)$$

where N is the total number of imaginary particles, and $x_n(t)$, $y_n(t)$, and $z_n(t)$ are the 3D coordinates of the walker's position at time t for the n th walker. $\langle \rangle$ indicates the average over all the particles. Since the mean square displacement $r^2(t)$ is proportional to time, the transport coefficient in the phase l , i.e., Γ_l , is related to the time derivative of $r^2(t)$ and the volume fraction of the phase V_l .

$$\Gamma_l = V_l \frac{1}{6} \frac{d\langle r^2(t) \rangle_l}{dt} \quad (4)$$

The mean square displacement in the porous media is lower than that obtained in a bulk material because the movement of the particles is interrupted at the phase boundaries. The degree of the reduction is measured quantitatively with the tortuosity factor τ_l , which is defined as

$$\tau_l = V_l \frac{I_l^{\text{bulk}}}{I_l^{\text{eff}}} = \frac{V_l}{V_l^{\text{eff}}} \frac{d\langle r^2(t) \rangle_l^{\text{bulk}}}{dt} / \frac{d\langle r^2(t) \rangle_l}{dt} \quad (5)$$

where V_l^{eff} is the volume fraction of the percolated cluster.

The anisotropic tortuosity factor is also evaluated using the directional mean square displacements $\langle x^2(t) \rangle$, $\langle y^2(t) \rangle$, and $\langle z^2(t) \rangle$, and a set of similar equations, namely, Eqs. (3)–(5).

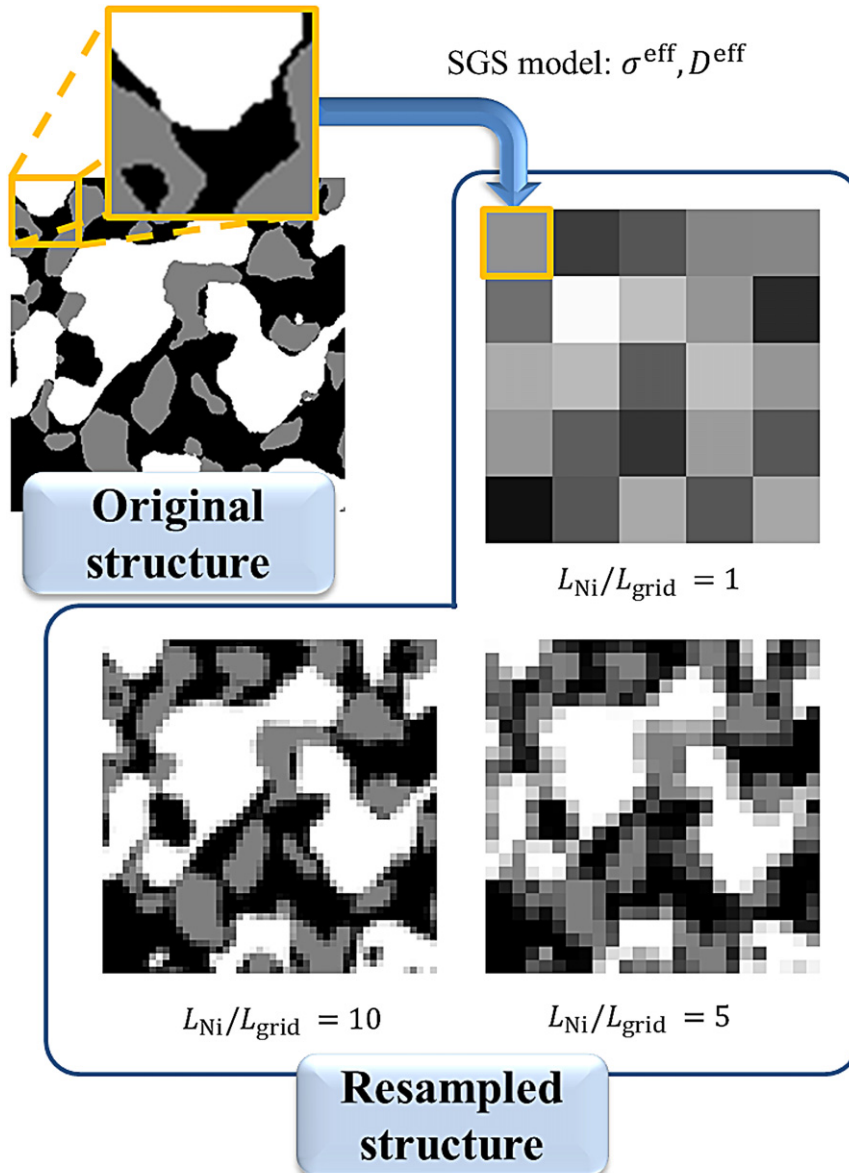


Fig. 2. Schematic diagram of the grid generation for the FVM analysis using the SGS models.

3.2. FVM-based diffusion simulation with the SGS model

3.2.1. Governing equation

To evaluate the structural complexity of the resampled structure used for the grid system, we conduct a simple diffusion simulation based on the FVM using the following equation.

$$\nabla \cdot (I_l^{\text{eff, local}} \nabla \phi_l) = 0 \quad (6)$$

where ϕ_l is an arbitrary potential, which corresponds to the electric potential or gas concentration in actual SOFC electrodes. $I_l^{\text{eff, local}}$ is the “local” transport coefficient, which is defined at every calculation grid and includes the local structural information evaluated by the SGS models. A detailed description of the SGS models is provided in the next section. We set the potential difference at the two facing edge surfaces of the calculation domain perpendicular to the Z axis and induce flux through the calculation domain (Fig. 3). From the amount of the induced flux, the effective transport

coefficient of the phase l , I_l^{eff} , in the whole calculation domain is obtained, and the tortuosity factor of the phase is subsequently obtained as follows:

$$\tau_l = V_l \frac{I_l^{\text{bulk}}}{I_l^{\text{eff}}} \quad (7)$$

3.2.2. Sub-grid-scale (SGS) model

To consider the structural information with a characteristic scale that is smaller than the calculation grid size and to evaluate $I_l^{\text{eff, local}}$, we have been developing SGS models and applying them to the simulation. In this study, we investigate four types of SGS models, the first two of which have already been reported in our previous work [14].

3.2.2.1. SGS1: Volume conservation. As the simplest SGS model, we consider the conservation of the phase volume in each grid (SGS1). The numbers of voxels corresponding to the Ni, YSZ, and pore

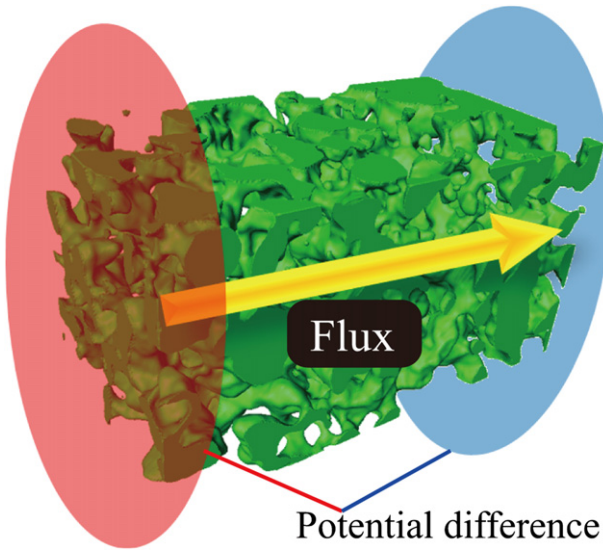


Fig. 3. Schematic picture of the FVM-based diffusion simulation.

phases are separately counted and the volume fractions are obtained. By using the volume fractions, the local transport coefficients $\Gamma_l^{\text{eff,local}}$ are evaluated in each grid as follows:

$$\Gamma_l^{\text{eff,local}} = V_l^{\text{local}} \Gamma_l^{\text{bulk}} \quad (8)$$

where Γ_l^{bulk} is the bulk transport coefficient and V_l^{local} is the volume fraction of the phase l in the grid.

In the FVM, any transport between two neighboring grids occurs through the interface they share. Since the local transport coefficients of the two grids are generally different, an averaged transport coefficient between the two grids needs to be evaluated to calculate the transport flux through the interface. Since an equally spaced grid system is used in this study, it is evaluated as a harmonic average of the effective transport coefficients of the two neighboring grids. The following formula shows the averaged effective transport coefficient between the grid (i, j, k) and grid $(i+1, j, k)$.

$$\Gamma_{l,(i+\frac{1}{2},j,k)}^{\text{eff,local}} = \left(\frac{1}{\Gamma_{l,(i,j,k)}^{\text{eff,local}}} + \frac{1}{\Gamma_{l,(i+1,j,k)}^{\text{eff,local}}} \right)^{-1} \quad (9)$$

Note that the LHS of eq. (9) is defined at the location of $i+1/2$, which corresponds to the interface of the grid (i, j, k) and grid $(i+1, j, k)$. The transport coefficients at the other interfaces are also defined with a similar formula.

3.2.2.2. *SGS2: Interfacial connectivity.* The coarser the grid becomes, the more difficult it becomes to capture the complex porous structure inside a grid only using the volume fraction of the porous components. The effect of the structural complexity on the transport phenomena should be considered in the grid. In the SGS model 2 (SGS2), the surface fraction of the conductive volume is evaluated on every grid interface and used to represent the structural complexity. First, the local transport coefficient in each grid is evaluated with eq. (8), and then the value at the interface is evaluated using the surface fractions of the conductive volume as follows.

$$\Gamma_{l,(i+\frac{1}{2},j,k)}^{\text{eff,local}} = \frac{S_{l,(i+\frac{1}{2},j,k)}}{S_{\text{all},(i+\frac{1}{2},j,k)}} \left(\frac{1}{\Gamma_{l,(i,j,k)}^{\text{eff,local}}} + \frac{1}{\Gamma_{l,(i+1,j,k)}^{\text{eff,local}}} \right)^{-1} \quad (10)$$

where S_{all} is the total surface area of the grid interface and S_l is the surface area of the phase l on the grid interface. The transport coefficients at the other interfaces are also defined with a similar formula. A more detailed description of the SGS2 can be found in our previous report [14].

3.2.2.3. *SGS3: Power law with a constant power index.* Before 3D observation of the porous structure became available with the help of FIB-SEM and X-ray CT technologies, porous models had been used to mimic the porous structure. In these models, the macroscopic tortuosity factor is often evaluated with the following empirical formula:

$$\Gamma_l^{\text{eff}} = V_l^\gamma \Gamma_l^{\text{bulk}} \quad (11)$$

where γ is the Bruggeman factor, which represents the state of the tortuous conduction paths inside the grids. A fully percolated network with a straight conduction path is represented as $\gamma=1$. Since the conduction path inside the porous structure is complicated and tortuous, the Bruggeman factor is over unity, and usually assumed to be 1.5–2.0 [25]. In the SGS3, we use the above macroscopic expression to evaluate the local tortuosity factor in each calculation grid (SGS3):

$$\Gamma_l^{\text{eff,local}} = (V_l^{\text{local}})^\gamma \Gamma_l^{\text{bulk}} \quad (12)$$

The volume fraction, V_l^{local} in eq. (12) is individually evaluated in each calculation grid, while V_l in eq. (11) is evaluated from the whole structure. Eq. (12) is equivalent to the following formula, where the local tortuosity factor term is shown explicitly:

$$\Gamma_l^{\text{eff,local}} = \frac{V_l^{\text{local}}}{\tau_l^{\text{local}}} \Gamma_l^{\text{bulk}}, \quad \tau_l^{\text{local}} = (V_l^{\text{local}})^{1-\gamma} \quad (13)$$

Here τ_l^{local} is the local tortuosity factor modeled by the SGS3. The local transport coefficient on a grid interface is evaluated with eq. (9). It should be noted that the SGS3 is equivalent to the SGS1 when the Bruggeman factor is unity.

3.2.2.4. *SGS4: Power law with an adaptive power index.* When the original porous structure is resampled to make a grid system, the heterogeneous nature inside the grid is significantly different in accordance with the grid size. When the grid size is larger, each grid can contain several solid particles so that relatively complicated transport path can be created inside the grid. On the other hand, when the grid size is smaller, each grid can contain only a part of the solid particles; hence the transport path inside the grid is less complicated. Therefore, it may be preferable to vary the effect of the SGS models depending on the grid size used in the simulation. In the SGS4, we consider the relationship between the grid size and the characteristic scale of the porous structure. In this sense, it is reasonable to include the length ratio L_l/L_{grid} into the SGS model. In this study, we vary the Bruggeman factor in the SGS3 depending on the ratio for further improvement of the SGS model.

The local transport coefficient and the local tortuosity factor are defined as follows:

Table 1

Sample sizes and voxel sizes.

Sample	Size [μm]			Voxel size [nm]		
	X	Y	Z	X	Y	Z
Ni:YSZ = 30:70	18.8	11.6	10.1	36.2	36.2	42.2
Ni:YSZ = 50:50	18.1	9.72	9.97	34.7	34.7	62.3
Ni:YSZ = 70:30	18.0	13.2	10.5	30.0	30.0	52.3

$$I_l^{\text{eff,local}} = \frac{V_l^{\text{local}}}{\tau_l^{\text{local}}} I_l^{\text{bulk}}$$

$$\tau_l^{\text{local}} = \left(V_l^{\text{local}} \right)^{1-\gamma} = \left(V_l^{\text{local}} \right)^{1-f} \left(\frac{L_l}{L_{\text{grid}}} \right) \quad (14)$$

where f is a function representing the dependency of γ on the length ratio. The derivation of the function is described in Section 4.

4. Results and Discussion

4.1. Microstructural parameters

Table 1 shows the sample sizes and voxel sizes of the anode samples. We successfully obtained a region larger than $10 \mu\text{m}^3$ for each anode sample, which is large enough to be representative of the whole anode structure as proved in our previous report [29]. **Table 2** shows the volume fraction of the anode samples. The ratios of the Ni and YSZ volume fractions, which are Ni:YSZ = 31.8:68.2, 53.5:46.5, and 69.1:30.9, respectively, are close to the intended values.

Table 3 shows the average particle/pore sizes measured by the line intercept method [33,34]. The values of the solid phases have a positive correlation with the volume fractions; a larger volume fraction causes more sintering between the same kinds of particles. The volume fraction of the pore phase depends on that of the Ni phase because a large part of the pore phase is created by the shrinkage of the NiO particles during the reduction. These particle/pore diameters are used as the characteristic scale of the porous component, L_l .

Table 4 shows the anisotropic tortuosity factors quantified by the random-walk simulation. Since some of the phases have no percolating cluster in a specific direction, tortuosity factors cannot be evaluated. Anisotropic aspects of the samples are weaker than those observed in our previous report [10], and the difference is attributed to the larger sample sizes, particularly in the Z direction. In the following discussion, the tortuosity factors in the Z direction are used as the reference values.

4.2. Diffusion simulation

Fig. 4 shows the tortuosity factors obtained by the FVM-based diffusion simulation with the SGS1, 2, and 3. The tortuosity factors are normalized with the reference values obtained by the random-walk simulation. The length ratio L_l/L_{grid} is used for the

Table 3

Average particle/pore sizes measured by the line intercept method.

Sample	Size [μm]		
	Ni	YSZ	Pore
Ni:YSZ = 30:70	1.34	1.74	1.39
Ni:YSZ = 50:50	1.87	1.35	1.55
Ni:YSZ = 70:30	2.55	1.11	2.19

horizontal axis. In every SGS model, the tortuosity factor converges to unity as the grid size becomes smaller. This indicates that the effect of the SGS models becomes smaller with finer grids and that the structural complexity can be represented simply by the grid-scale information. In the case of coarser grids, on the other hand, only grid-scale information is not enough; hence, the sub-grid-scale information contributes significantly to the representation of the structural complexity. However, since the method of evaluating sub-grid-scale information is different among the SGS models, the trends of $\tau_{\text{SGS}}/\tau_{\text{RW}}$ are significantly different.

First, in the SGS1, the values of $\tau_{\text{SGS}}/\tau_{\text{RW}}$ monotonically increase to unity as the grid size becomes smaller, which is the same trend that is observed in our previous report [14]. The tortuosity factors are significantly underestimated in the case of coarser grids, indicating that only volume conservation is not enough to represent the structural complexity inside the grid. We need to evaluate a higher-order quantity associated with the heterogeneous nature of the porous structure for more sophisticated SGS model.

Secondly, in the SGS2, the local structural complexity is evaluated with the surface information of the grids. This approach results in drastic changes in the trends of $\tau_{\text{SGS}}/\tau_{\text{RW}}$. The values of $\tau_{\text{SGS}}/\tau_{\text{RW}}$ approach unity even in the case of coarser grids. Similar results were also obtained in our previous report [14]. However, the extent of the effect is different from phase to phase. For example, in the YSZ phase of the Ni:YSZ = 30:70 anode, the tortuosity factors are reasonably evaluated over a wide range of grid sizes. On the other hand, in the YSZ phase of the Ni:YSZ = 70:30 anode, the value is significantly overestimated in the intermediate grid size region ($L_l/L_{\text{grid}} \sim 5$). These unsystematic behaviors of the SGS2 can be attributed to the fact that the relationships between the surface information and the inner information are not straightforward. Therefore, the SGS2 may not always be valid in a wide variety of porous structures.

Thirdly, in the SGS3, the structural complexity inside a grid is evaluated by the volume fraction and Bruggeman factor γ , whose value is set to 1.2, 1.5, or 1.8 in this study. This approach is to employ the macroscopic expression used in the conventional porous models (Eq. (11)) on the evaluation of the local tortuosity factor (Eq. (12)). When the value of γ is small, the structural complexity is still underestimated in the coarser grid size region; the trends observed in the graph are similar to that in the SGS1. However, simply increasing the value of γ is not an effective solution; the structural complexity tends to be overestimated in the case of intermediate grids if a larger γ is applied. We found that it was impossible to properly represent the structural complexity over a wide range of grid sizes if a constant value is applied for γ .

Table 4

Anisotropic tortuosity factors quantified by random-walk simulation.

Sample	Ni			YSZ			Pore		
	X	Y	Z	X	Y	Z	X	Y	Z
Ni:YSZ = 30:70	—	78.30	—	1.71	1.57	2.57	6.17	3.92	10.82
Ni:YSZ = 50:50	4.91	3.43	3.79	7.93	5.63	5.39	3.48	3.04	2.64
Ni:YSZ = 70:30	2.79	2.41	1.85	—	—	14.05	3.26	2.71	2.27

Table 2

Volume fractions.

Sample	Volume fractions [%]		
	Ni	YSZ	Pore
Ni:YSZ = 30:70	23.6	50.6	25.8
Ni:YSZ = 50:50	34.2	29.7	36.1
Ni:YSZ = 70:30	42.3	18.9	38.8

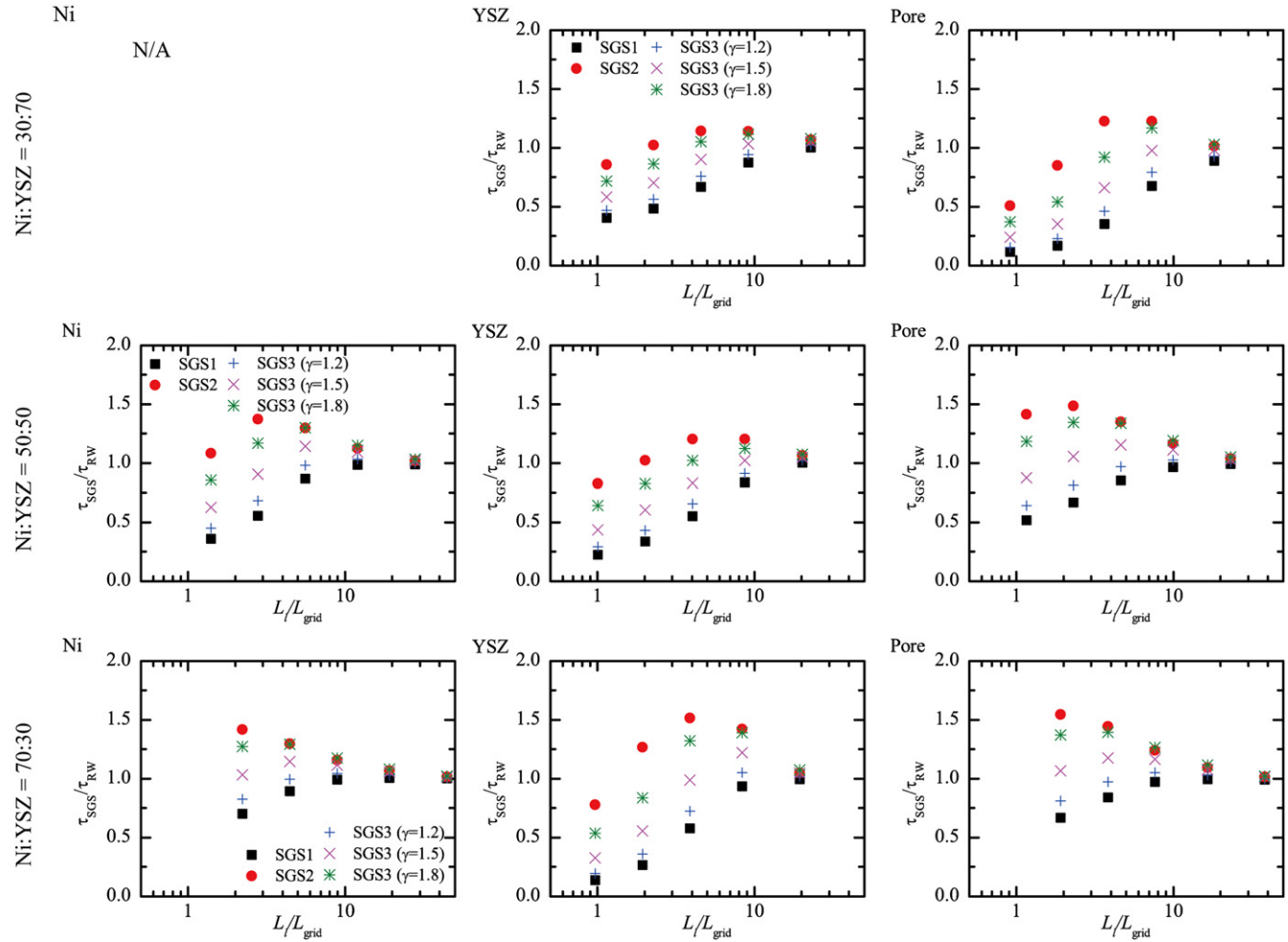


Fig. 4. Tortuosity factors obtained by the FVM-based diffusion simulation normalized by the reference tortuosity factors obtained by the random-walk simulation.

The SGS1, 2, and 3 discussed above showed positive contributions to maintain the structural information in the resampled structure used as the calculation grid system. However, they are not always valid in a wide range of grid sizes; underestimation or overestimation is often observed. This is because the same formula is applied to all grid sizes. The heterogeneous nature inside the grid significantly varies with the grid sizes so that a tuning parameter is required to vary the effect of the SGS model depending on the grid size. This is the motivation to consider the Bruggeman factor γ as an adaptive power index in the SGS4.

In the last model, we estimate the local tortuosity factor with an adaptive power index γ which depends on the ratio of the characteristic length L_l and the grid size L_{grid} . In order to decide the dependency of γ on the length ratio L_l/L_{grid} we regard γ as a fitting parameter and find its appropriate value γ^0 with which the macroscopic structural complexity is properly evaluated; in other words, the value of $\tau_{\text{SGS}}/\tau_{\text{RW}}$ becomes unity. Fig. 5 shows the required value of γ^0 for each phase versus the length ratio L_l/L_{grid} . The calculation is conducted in all the phases in all the samples except the Ni phase of the Ni:YSZ = 30:70 sample. Although there is some deviation, the graph reveals an apparent trend. If the value of L_l/L_{grid} is large enough or the grid size is small enough, γ^0 converges to unity. This indicates that the structural complexity of the porous structure is represented by the grid-scale information and that we do not need to rely on the sub-grid-scale information in conducting the transport analysis. On the other hand, if the value of L_l/L_{grid} becomes smaller or the grid size becomes larger, γ^0 tends to steeply

increase up to around 2.5. This result gives us an important criterion in making a calculation grid system. If the characteristic length of the porous structure (e.g. particle/pore diameter) is represented with more than 15 grids, the structural information of the porous electrodes can be represented by the grid-scale information. Otherwise, the SGS model should be applied to the resampled structure to maintain the quality of the structural information. In the anode overpotential analysis, where we need to consider the transports in the three phases at the same time, the allowable maximum grid size without the SGS model is determined by the structure that has the smallest characteristic scale. For the Ni:YSZ = 30:70, 50:50, and 70:30 anodes used in this study, the grid

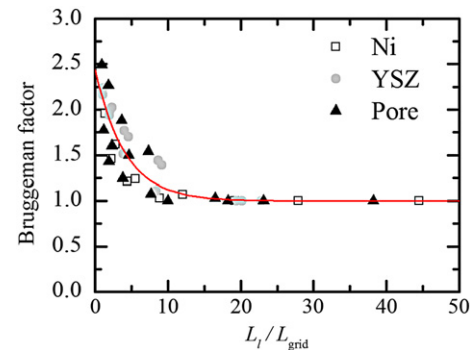


Fig. 5. Required Bruggeman factor against the length ratio, L_l/L_{grid} , and its fitted curve.

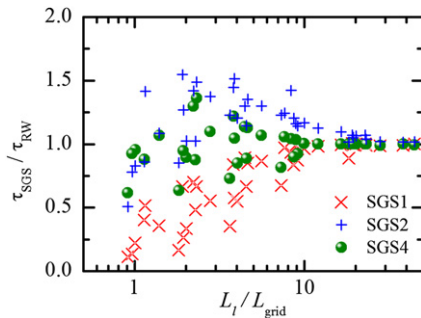


Fig. 6. Comparison of the three types of SGS models.

size needs to be smaller than 89, 90, and 74 nm, respectively. However, it is not always possible to use such small grid sizes when we consider reasonable computational resources, so that the aid of the SGS model is significantly important.

Considering the value of the Bruggeman factor must be larger than unity, we fit the obtained values of γ^0 on the following exponential formula.

$$\gamma = A \exp\left(-\lambda \frac{L_l}{L_{\text{grid}}}\right) + 1 \quad (15)$$

where A is a pre-exponential factor and λ is a decay constant. The solid line in Fig. 5 is the fitting curve, where $A = 1.44$ and $\lambda = 0.246$. The mean square deviation is 0.832. It is worth noting the structure data used in the fitting: the volume fraction of the phase is from 18.9 to 50.6%, which covers structures both over and below the percolation threshold of ordinary porous materials. The particle/pore size is from 1.11 to 2.55 μm , which is typical for an SOFC electrode material.

Fig. 6 shows the comparison of the effects among the various SGS models. All values of $\tau_{\text{SGS}}/\tau_{\text{RW}}$ obtained in all the phases of all the samples are summarized in the graph. It can be seen that the SGS4 succeeds in making the $\tau_{\text{SGS}}/\tau_{\text{RW}}$ much closer to unity than the other models. Structural complexity in coarser grid cases is more accurately represented than the SGS1, and the overshoot seen in the SGS2 is moderated. Although the SGS4 does not give perfect values for in all $\tau_{\text{SGS}}/\tau_{\text{RW}}$ grid size cases, significant improvement is achieved. The attempt to include the effect of L_l/L_{grid} in the SGS model has a positive contribution to developing a more sophisticated SGS model.

The computation time required to obtain a convergent solution with the SGS4 is shown in Fig. 7. All computation times are measured when using a single core of Xeon W3690 processor. It clearly shows the effectiveness of the SGS model. If a coarser grid can be used in the electrode simulation without losing accuracy, the electrode simulation can be applied to a larger-scale analysis, or we

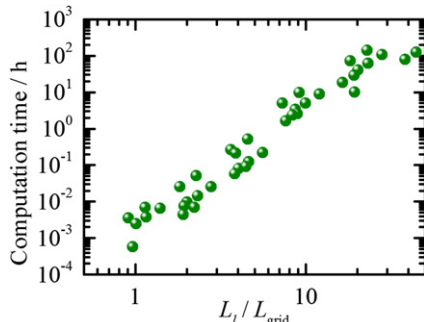


Fig. 7. Computation time required to obtain a convergent solution when the SGS4 is applied.

can expect more accuracy in the simulation with limited computational resources.

5. Conclusions

Improving the accuracy of the sub-grid-scale model used for the 3D numerical analysis in the SOFC electrode is accomplished by introducing an adaptive power index. Four types of SGS models are applied to the transport analysis to clarify their effect and applicability. Although the first three models, namely, volume conservation, interfacial connectivity, and the power law with a constant power index models, have a positive contribution to maintain the structural information in the resampled structure used for the grid system, their applicability is not completely assured in a wide range of grid sizes. In the last model, we introduce an adaptive power index to the power-law-type model to let the model exert its effect appropriately in accordance with the grid size. When the length ratio between the grid size and the characteristic scale of the original structure is adopted as an adaptive power index, the model succeeds in representing the original structural information in wide a range of grid sizes and reducing the computational cost without losing simulation accuracy. An accurate and effective SGS model can promote a flexible application of the numerical technique to the analysis in porous materials.

Acknowledgments

This work was supported by Grant-in-Aid for JSPS Fellows Grant Number 10J01318, and the New Energy and Industrial Technology Development Organization (NEDO) under the Development of System and Elemental Technology on Solid Oxide Fuel Cell (SOFC) Project.

Nomenclature

A	pre-exponential factor
L	length (m)
r	non-dimensional displacement
S	surface area (m^2)
V	volume fraction

Greek symbols

γ	Bruggeman factor
Γ	transport coefficient
λ	decay constant
τ	tortuosity factor
ϕ	arbitrary potential

Subscripts

i	coordinate number in x direction
j	coordinate number in y direction
k	coordinate number in z direction
l	phase

Superscripts

bulk	value for bulk material
eff	value for porous material
local	local value defined in a calculation grid

References

- [1] T. Matsui, R. Kishida, J.-Y. Kim, H. Muroyama, K. Eguchi, Journal of the Electrochemical Society 157 (5) (2010) B776–B781.
- [2] H. Sumi, R. Kishida, J.-Y. Kim, H. Muroyama, T. Matsui, K. Eguchi, Journal of the Electrochemical Society 157 (12) (2010) B1747–B1752.

- [3] L. Holzer, B. Iwanschitz, Th. Hocker, B. Münch, M. Prestat, D. Wiedenmann, U. Vogt, P. Holtappels, J. Sfeir, A. Mai, Th. Graule, *Journal of Power Sources* 196 (2011) 1279–1294.
- [4] J.S. Cronin, J.R. Wilson, S.A. Barnett, *Journal of Power Sources* 196 (2011) 2640–2643.
- [5] M. Shah, P.W. Voorhees, S.A. Barnett, *Solid State Ionics* 187 (2011) 64–67.
- [6] J.R. Wilson, J.S. Cronin, S.A. Barnett, *Scripta Materialia* 65 (2011) 67–72.
- [7] M.H. Pihlatie, A. Kaiser, M. Mogensen, M. Chen, *Solid State Ionics* 189 (2011) 82–90.
- [8] P.R. Shearing, Q. Cai, J.I. Golbert, V. Yufit, C.S. Adjiman, N.P. Brandon, *Journal of Power Sources* 195 (2010) 4804–4810.
- [9] N. Shikazono, D. Kanno, K. Matsuzaki, H. Teshima, S. Sumino, N. Kasagi, *Journal of the Electrochemical Society* 157 (5) (2010) B665–B672.
- [10] M. Kishimoto, H. Iwai, M. Saito, H. Yoshida, *Journal of Power Sources* 196 (2011) 4555–4563.
- [11] M. Kishimoto, H. Iwai, M. Saito, H. Yoshida, *Proceedings of the 14th International Heat Transfer Conference, IHTC-22495*, 2010.
- [12] K. Matsuzaki, N. Shikazono, N. Kasagi, *Journal of Power Sources* 196 (2011) 3073–3082.
- [13] Q. Cai, C.S. Adjiman, N.P. Brandon, *Electrochimica Acta* 56 (2011) 10809–10819.
- [14] M. Kishimoto, H. Iwai, M. Saito, H. Yoshida, *Journal of the Electrochemical Society* 159 (3) (2012) B315–B323.
- [15] J. Mizusaki, H. Tagawa, T. Saito, T. Yamamura, K. Kamitani, K. Hirano, S. Ehara, T. Takagi, T. Hikita, M. Ippommatsu, S. Nakagawa, K. Hashimoto, *Solid State Ionics* 70/71 (1994) 52–58.
- [16] B. de Boer, Ph.D. Thesis, University of Twente, Netherlands, 1998.
- [17] A. Bieberle, L.P. Meier, L.J. Gauckler, *Journal of the Electrochemical Society* 148 (6) (2001) A646–A656.
- [18] A. Utz, H. Störmer, A. Leonide, A. Weber, E. Ivers-Tiffée, *Journal of the Electrochemical Society* 157 (6) (2010) B920–B930.
- [19] R. Radhakrishnan, A.V. Virkar, S.C. Singhal, *Journal of the Electrochemical Society* 152 (1) (2005) A210–A218.
- [20] T. Kawada, N. Sakai, H. Yokokawa, M. Dokuya, *Journal of the Electrochemical Society* 137 (10) (1990) 3042–3047.
- [21] Y. Suzue, N. Shikazono, N. Kasagi, *Journal of Power Sources* 184 (2008) 52–59.
- [22] H. Zhu, R.J. Kee, V.M. Janardhanan, O. Deutschmann, D.G. Goodwin, *Journal of the Electrochemical Society* 152 (12) (2005) A2427–A2440.
- [23] W.G. Bessler, M. Volger, H. Störmer, D. Gerthsen, A. Utz, A. Weber, E. Ivers-Tiffée, *Physical Chemistry Chemical Physics* 12 (2010) 13888–13903.
- [24] P. Costamagna, P. Costa, V. Antonucci, *Electrochimica Acta* 43 (1998) 375–394.
- [25] J.H. Nam, D.H. Jeon, *Electrochimica Acta* 51 (2006) 3446–3460.
- [26] A. Abbaspour, J.-L. Luo, N. Nandakumar, *Electrochimica Acta* 55 (2010) 3944–3950.
- [27] J.R. Wilson, W. Kobsiriphat, R. Mendoza, H.-Y. Chen, J.M. Hiller, D.J. Miller, K. Thornton, P.W. Voorhees, S.B. Adler, S.A. Barnett, *Nature Material* 5 (7) (2006) 541–544.
- [28] P.R. Shearing, J. Golbert, R.J. Chater, N.P. Brandon, *Chemical Engineering Science* 64 (17) (2009) 3928–3933.
- [29] H. Iwai, N. Shikazono, T. Matsui, H. Teshima, M. Kishimoto, R. Kishida, D. Hayashi, K. Matsuzaki, D. Kanno, M. Saito, H. Muroyama, K. Eguchi, N. Kasagi, H. Yoshida, *Journal of Power Sources* 195 (2010) 955–961.
- [30] D. Gostovic, J.R. Smith, D.P. Kundinger, K.S. Jones, E.D. Wachsman, *Electrochemical and Solid-State Letters* 10 (12) (2007) B214–B217.
- [31] N. Vivet, S. Chupin, E. Estrade, T. Piquero, P.L. Pommier, D. Rochais, E. Bruneton, *Journal of Power Sources* 196 (2011) 7541–7549.
- [32] Y. Nakashima, S. Kamiya, *Journal of Nuclear Science and Technology* 44 (9) (2007) 1233–1247.
- [33] D. Simwonis, F. Tietz, D. Stömer, *Solid State Ionics* 132 (2000) 241–251.
- [34] J.-H. Lee, H. Moon, H.-W. Lee, J. Kim, J.-D. Kim, K.-H. Yoon, *Solid State Ionics* 148 (2002) 15–26.